A DAE SOLVER FOR COORDINATION OF FORCE-CONTROLLED HYBRID TESTING

Frederik Nordtorp[*1] and Giuseppe Abbiati[1]

[1]Department of Civil and Architectural Engineering, Aarhus University, Inge Lehmanns Gade 10, Aarhus, 8000, Denmark. [*]Corresponding author. Email: fnk@cae.au.dk

Preprint notice. This manuscript is a preprint and has not been peer reviewed. It is the author-submitted version made publicly available on engrXiv prior to journal peer review.

ABSTRACT

Hybrid testing couples numerical simulation with physical experiments by enforcing compatibility and equilibrium at the interface between numerical and physical substructures. This paper presents a force-controlled hybrid-testing formulation for stiff physical substructures coupled to nonlinear numerical substructures. Displacement compatibility is imposed directly on the numerical equations of motion to form a differential-algebraic equation. The interface force is obtained using Baumgarte-stabilized Lagrange multipliers. Physical-substructure velocity and acceleration, which are not measured in pseudo-dynamic testing, are estimated from displacement feedback using cubic regression. A linear illustrative system is used to assess convergence, stability, numerical damping, and period distortion for explicit time-integration schemes. The formulation is then demonstrated experimentally by coupling a stiff axially loaded steel-bar physical substructure to a nonlinear two-degree-of-freedom numerical substructure with a Duffing-type spring. The hybrid test remains stable, reproduces the dominant simulated dynamics, and maintains displacement compatibility despite noisy camera-based displacement feedback. These results show that Baumgarte-stabilized constraint dynamics provide a practical strategy for force-controlled hybrid testing of stiff physical substructures.

INTRODUCTION

Background and motivation

Hybrid testing (HT) combines numerical simulation and physical testing by partitioning a system into a numerical substructure (NS) and a physical substructure (PS). Since its early developments (Hakuno et al. 1969; Takanashi et al. 1975), HT has been widely used in seismic testing (Pan et al. 2016; Saouma and Sivaselvan 2014) and extended to fire (Sauca et al. 2021), hydrodynamic (Neumann et al. 2023), aerodynamic (Su and Song 2019), and multi-actuator applications (Fermandois and Spencer 2017; Silva et al. 2020; Abbiati et al. 2015). When the PS response is rate independent, HT can be coordinated in a pseudo-dynamic regime, where the physical test is executed slower than the simulated structural response.

A coordination algorithm imposes force equilibrium and displacement compatibility between PS and NS. The commanded interface quantities and measured PS responses are realized through a transfer system that includes the actuators, sensors, controllers, and measurement systems. Coordination algorithms can be broadly classified as simulation-based or control-based. The former are derived from numerical schemes used to solve ODEs/DAEs (Kolay et al. 2015; Jia et al. 2011; Bursi et al. 2013), while the latter are formulated as solutions to control problems (Silva et al. 2020; Carrion and Spencer 2007; Liu et al. 2024a; Christenson et al. 2008; Ou et al. 2015; Zhou et al. 2017). Most HT implementations use displacement control, in which interface displacements are imposed on the PS and measured interface forces are returned to the NS.

Displacement control, however, becomes impractical when the PS stiffness is close to the loading-system stiffness, since small displacement disturbances propagate to large fluctuations in the restoring force. Several force-control strategies have therefore been proposed. (Dimig et al. 1999) introduced Effective Force Testing (EFT), in which a prescribed effective force reproduces the structural response to ground motion. (Zhao et al. 2005) improved EFT by adding velocity feedback compensation to increase force-tracking accuracy. (Forouzan and Nakata 2015) proposed a predictor–corrector algorithm for force-controlled HT to improve robustness and response accuracy. (Pratt and Krupp 2004) achieved force control by adding mechanical compliance to the actuator

loop, allowing the applied force to be inferred from Hooke's law, although this requires additional physical hardware.

Other methods improve force tracking by modifying the actuator–structure interaction. Sivaselvan et al. (Sivaselvan et al. 2008) proposed dynamic force control using added compliance and displacement compensation through transfer-function representations. This approach was developed for stiff structures, but can become sensitive to changes in structural properties during testing. (Carl and Sivaselvan 2011) addressed related stability issues using an impedance-based feedforward scheme that modifies the apparent interaction between the actuator and the tested structure. (Stefanaki and Sivaselvan 2018) proposed a simplified dynamic substructuring framework that separates the substructuring controller from the PS dynamics and reduces the need for explicit tracking-controller design. (Verma et al. 2019) introduced an impedance-matching strategy in which the transfer system is modeled with a control input, a reaction-force input, and a displacement output.

Although these methods have advanced force-controlled HT, many rely on linearized models and transfer functions. Such assumptions are restrictive for nonlinear systems. As an example, this limitation is increasingly relevant for geometric nonlinearities (Sauder et al. 2016; Belloli et al. 2020; Zhang et al. 2016; Ding et al. 2024; Herrmann et al. 2012; Shao et al. 2021; Guo et al. 2021; Liu et al. 2024b; Witteveen and Koller 2023) and material nonlinearities (Chen et al. 2024; Bas and Moustafa 2020a; Bas and Moustafa 2020b; Mosqueda and Ahmadizadeh 2011).

Scope

This paper proposes a DAE-based coordination algorithm for hybrid testing with force-controlled physical-substructure degrees of freedom. DAE solvers provide an alternative by coupling the PS and NS ODEs through algebraic interface constraints (Jia et al. 2011; Bursi et al. 2013). In the proposed approach, displacement compatibility is imposed directly on the equations of motion of the NS, and the corresponding interface force is obtained from Baumgarte-stabilized Lagrange multipliers. The computed interface force is used as the actuator force command, enabling force-controlled coupling of a stiff PS to a nonlinear NS. The formulation is assessed using a linear

stability benchmark and demonstrated experimentally on a stiff physical substructure coupled to a nonlinear numerical model.

The paper is organized as follows. Section 1 introduces the background, motivation, and scope. Section 2 presents the force-controlled hybrid-testing framework. Section 3 introduces a linear illustrative hybrid system used to examine the numerical behavior of the proposed formulation. Section 4 presents the convergence, stability, damping, and period-distortion analyses. Section 5 describes the nonlinear hybrid-test case study with a stiff physical substructure and the corresponding experimental setup. Section 6 presents and discusses the hybrid-test results, and Section 7 concludes the work.

FORCE-CONTROLLED HYBRID TESTING FRAMEWORK

A coordination algorithm, which may take the form of either a time-integration or control scheme, ensures that the NS and PS satisfy equilibrium and coupling conditions (for example, displacement compatibility). In most work related to HT, the PS is tested in displacement-control mode, as illustrated in Fig. 1a.

When coordinating an HT in displacement-control mode, the interface displacement between the NS and PS is obtained at each timestep by integrating the state-space equations of the NS using a suitable time-integration scheme. This displacement is sent as a command to an actuation system, ensuring displacement compatibility between the two substructures. On the PS, the corresponding interface force is measured using load cells and subsequently fed back to the NS to maintain equilibrium in the next timestep.

Displacement control is, however, problematic when the PS has a stiffness of a similar order of magnitude as that of the actuation system. In such configurations, the interface is typically subjected to small displacements, making the compliance of the actuation system and the noise in feedback signals non-negligible. Testing the PS in force-control mode addresses this issue. In this mode, a force command is sent to the actuation system, and once equilibrium is achieved, the measured displacement feedback is returned to the NS. The coordination algorithm for force-controlled HT is illustrated in Fig. 1b.

Despite its advantages for testing a stiff PS, force-control introduces several difficulties for the NS. In this configuration, the NS receives a displacement and must return a corresponding force, which cannot be solved with forward dynamics. This inverse problem is often addressed using transfer functions, but such an approach is difficult for nonlinear systems.

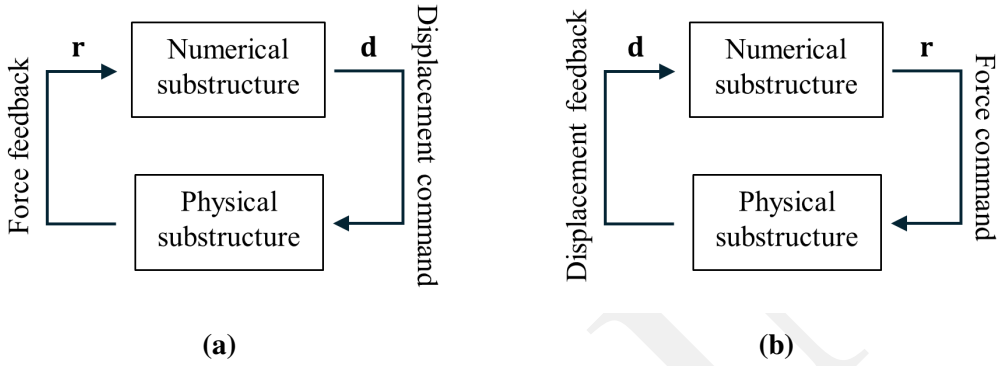

Fig. 1. Hybrid testing schemes for (a) displacement control mode and (b) force control mode.

In this setting, displacement compatibility is enforced as an algebraic constraint on the NS dynamics to form the differential algebraic equation (DAE),

$$\begin{cases} \dot{\mathbf{q}} = \mathbf{u} \\ \dot{\mathbf{u}} = -\mathbf{M}^{-1}(\mathbf{f} - \mathbf{h}^T\mathbf{r}) \\ \mathbf{hq} = \mathbf{d} \end{cases} \tag{1}$$

where $\mathbf{q}$ contains the NS degrees of freedom, $\mathbf{u}$ contains their time derivatives, t is the simulation time, and $\dot{(\cdot)}$ denotes a time derivative. The mass matrix $\mathbf{M}$ and force vector $\mathbf{f}$ are obtained from the NS dynamics. The matrix $\mathbf{h}$ maps the NS degrees of freedom to the PS displacement feedback $\mathbf{d}$, and $\mathbf{r}$ is the interface force represented by the Lagrange multiplier.

Various numerical methods exist for solving DAEs. (Ascher and Petzold 1998) suggest, among others, half-implicit and projection-based Runge-Kutta methods. However, these approaches are effective only for prescribed constraints, as they exhibit instability within feedback loops. Additionally, they often require iterations, which is problematic in a HT setting. Alternatively, as the

system in (1) is a Hessenberg index-2 DAE, it can be reduced to an ODE. Here the index refers to the number of differentiations required to eliminate algebraic constraints. Differentiating the constraint yields,

$$\mathbf{g} = \mathbf{hq} - \mathbf{d} = \mathbf{0} \tag{2}$$

$$\dot{\mathbf{g}} = \mathbf{hu} - \dot{\mathbf{d}} = \mathbf{0} \tag{3}$$

$$\ddot{\mathbf{g}} = -\mathbf{hM}^{-1}\mathbf{f} + \mathbf{hM}^{-1}\mathbf{h}^T\mathbf{r} - \ddot{\mathbf{d}} = \mathbf{0} \tag{4}$$

From (4), the interface force $\mathbf{r}$ can be determined and substituted into (1), reducing the system to an ODE. However, enforcing the constraint at the acceleration level alone leads to drift in position and velocity, compromising stability over time.

To mitigate this issue, Baumgarte stabilization (Baumgarte 1972) is applied by forming a weighted combination of (2), (3), and (4),

$$\ddot{\mathbf{g}} + 2\alpha\dot{\mathbf{g}} + \beta^2\mathbf{g} = \mathbf{0} \tag{5}$$

where α and β are Baumgarte stabilization parameters that control the damping and stiffness of the constraint-error correction. Choosing $\alpha = \beta$ gives critical damping of the error dynamics. Larger values reduce constraint drift more aggressively, but can also increase sensitivity to noisy displacement feedback. The Baumgarte parameters are therefore treated as algorithmic tuning parameters rather than physical properties of the system, and their influence is examined explicitly in the stability analysis.

Solving for the interface force $\mathbf{r}$ in (5) yields the expression,

$$\mathbf{r} = -(\mathbf{hM}^{-1}\mathbf{h}^T)^{-1}(-\mathbf{hM}^{-1}\mathbf{f} - \ddot{\mathbf{d}} + 2\alpha(\mathbf{hu} - \dot{\mathbf{d}}) + \beta^2(\mathbf{hq} - \mathbf{d})) \tag{6}$$

which is used to transform the DAE of (1) into the ODE,

$$\begin{cases} \dot{\mathbf{q}} = \mathbf{u} \\ \dot{\mathbf{u}} = -\mathbf{M}^{-1}(\mathbf{f} + \mathbf{h}^T(\mathbf{h}\mathbf{M}^{-1}\mathbf{h}^T)^{-1}(-\mathbf{h}\mathbf{M}^{-1}\mathbf{f} - \ddot{\mathbf{d}} + 2\alpha(\mathbf{h}\mathbf{u} - \dot{\mathbf{d}}) + \beta^2(\mathbf{h}\mathbf{q} - \mathbf{d}))) \end{cases} \tag{7}$$

Introducing the state vector $\mathbf{x} = \begin{bmatrix} \mathbf{q} & \mathbf{u} \end{bmatrix}^T$, (7) can be reduced to,

$$\dot{\mathbf{x}} = \mathbf{f}^{rhs}(\mathbf{x}, \mathbf{d}, \dot{\mathbf{d}}, \ddot{\mathbf{d}}) \tag{8}$$

However, in pseudo-dynamic hybrid tests, the velocity $\dot{\mathbf{d}}$ and acceleration $\ddot{\mathbf{d}}$ of the PS are not directly measurable and must therefore be estimated. At each time step i, a cubic polynomial approximation of the PS displacement is constructed.

Algorithm 1 summarizes the proposed force-controlled coordination scheme. Each Runge–Kutta stage uses the available PS displacement history to estimate $\dot{\mathbf{d}}$ and $\ddot{\mathbf{d}}$, compute the Baumgarte-stabilized interface force, send the force command, and update the NS state from the returned displacement feedback.

Algorithm 1 Force-Controlled Hybrid Testing with Runge–Kutta Integration

Initialize $\mathbf{q}_1, \ldots, \mathbf{q}_n$, $\mathbf{u}_1, \ldots, \mathbf{u}_n$ and $\mathbf{d}_1, \ldots, \mathbf{d}_n$
for $i = n, n+1, \ldots, N_{\text{steps}} - 1$ **do** ▷ Time-stepping loop
  for $j = 1, \ldots, s$ **do** ▷ Runge–Kutta stages loop
    Update stage $\mathbf{x}_{i,j} \leftarrow \mathbf{x}_i + \Delta t \sum_{k=1}^{j-1} a_{j,k} \dot{\mathbf{x}}_{i,k}$
    Estimate velocity $\dot{\tilde{\mathbf{d}}}_{i,j}(t_i)$ and acceleration $\ddot{\tilde{\mathbf{d}}}_{i,j}(t_i)$
    Compute interface force $\mathbf{r}_{i,j}$ from (6)
    Send force command $\mathbf{r}_{i,j}$
    Get displacement feedback $\mathbf{d}_{i,j}$
    Evaluate stage derivative $\dot{\mathbf{x}}_{i,j}$ from (8)
  end for
  Update state $\mathbf{x}_{i+1} \leftarrow \mathbf{x}_i + \Delta t \sum_{j=1}^{s} b_j \dot{\mathbf{x}}_{i,j}$
  Update time $t_{i+1} \leftarrow t_i + \Delta t$
end for

Here, s denotes the number of Runge–Kutta stages, $a_{j,k}$ and b_j are the Runge–Kutta coefficients, N_{steps} is the number of time steps, and n is the number of previous states retained for the derivative

estimation.

The PS is engaged at every Runge–Kutta stage, producing multiple force–displacement exchanges within each timestep. Since the force command depends on the measured displacement feedback and the estimated PS derivatives, the stability and accuracy depend on the integration scheme, Baumgarte parameters, and regression procedure. These effects are examined next using a linear illustrative hybrid system.

LINEAR ILLUSTRATIVE HYBRID TEST

To illustrate the proposed framework, a simple linear hybrid system is considered. The system consists of a single-degree-of-freedom NS coupled to a PS, as shown in Fig. 2. The NS comprises a rigid body of mass $m = 0.5\ kg$ attached to a linear spring with stiffness $k_{NS} = 0.39\ N/mm$, where the motion is described by the translational degree of freedom q. The PS is connected to the mass and is realized as a spring.

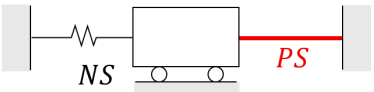

Fig. 2. Hybrid model of illustrative example, where the physical substructure (PS) is highlighted in red and the numerical substructure is in black.

The hybrid model is decomposed into a free-body diagram, revealing the interface force. The resulting NS and PS are shown in Fig. 3a and -b, respectively.

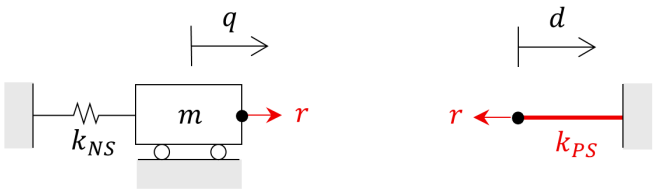

Fig. 3. Free-body diagrams of the decomposed linear hybrid model showing a) the numerical substructure and b) the physical substructure. The interface force r couples the two substructures, and d is the PS displacement.

The dynamics of the NS are governed by,

$$m\ddot{q} + k_{NS}q - r = 0 \tag{9}$$

where r is the interface force between NS and PS, represented by a Lagrange multiplier to ensure displacement compatibility $q = d$ between the two substructures.

Following the form of (1), the coupled system is written as,

$$\begin{cases} \dot{q} = u \\ \dot{u} = -\frac{1}{m}(k_{NS}q - r) \\ q = d \end{cases} \tag{10}$$

Applying the Baumgarte-stabilized constraint solution from (6) gives the interface force,

$$r = k_{NS}q + m(\ddot{d} + 2\alpha(\dot{d} - u) + \beta^2(d - q)) \tag{11}$$

Substitution of (11) into (10) eliminates the algebraic constraint and gives the ODE,

$$\begin{cases} \dot{q} = u \\ \dot{u} = \ddot{d} + 2\alpha(\dot{d} - u) + \beta^2(d - q) \end{cases} \tag{12}$$

For this single-DOF example, the mechanical dynamics are absorbed into the interface force. The remaining ODE describes a stabilized constraint motion, with PS-acceleration feedforward and PD-type Baumgarte correction of the compatibility error.

The linear illustrative example is evaluated numerically using a virtual PS. The PS is modeled as a linear spring, such that,

$$d = \frac{1}{k_{PS}} r \tag{13}$$

where $k_{PS} = 0.39$ N/mm is the assumed PS stiffness.

The proposed framework is not restricted to a specific scheme for estimating the PS velocity and acceleration. In the present implementation, these quantities are obtained from a local cubic reconstruction of the displacement history,

$$\dot{d}_i = \frac{\mathrm{d}}{\mathrm{d}t} f(t)\bigg|_{t=t_i}, \quad \ddot{d}_i = \frac{\mathrm{d}^2}{\mathrm{d}t^2} f(t)\bigg|_{t=t_i} \tag{14}$$

where i denotes the current timestep and $f(t)$ is the reconstructed PS displacement trajectory, given by,

$$f(t) = a_3 t^3 + a_2 t^2 + a_1 t + a_0 \tag{15}$$

The coefficients a_3, a_2, a_1 and a_0 are determined by a least-squares fit to the known displacement and velocity history, augmented by the current displacement,

$$\mathbf{a} = \arg\min_{\mathbf{a}} \left\| \begin{bmatrix} f(t_i) - d_i \\ f(t_{i-1}) - q_{i-1} \\ f(t_{i-2}) - q_{i-2} \\ f(t_{i-3}) - q_{i-3} \\ \frac{\mathrm{d}}{\mathrm{d}t} f(t_{i-1}) - u_{i-1} \\ \frac{\mathrm{d}}{\mathrm{d}t} f(t_{i-2}) - u_{i-2} \\ \frac{\mathrm{d}}{\mathrm{d}t} f(t_{i-3}) - u_{i-3} \end{bmatrix} \right\| \tag{16}$$

where $\mathbf{a} = \begin{bmatrix} a_3 & a_2 & a_1 & a_0 \end{bmatrix}^T$. The resulting history-dependent discrete-time formulation is expressed through the augmented state vector,

$$\mathbf{x}_i = \begin{bmatrix} \mathbf{q}_{i-1} & \dots & \mathbf{q}_{i-n} & \mathbf{u}_{i-1} & \dots & \mathbf{u}_{i-n} & \mathbf{d}_i \end{bmatrix}^T \tag{17}$$

Here, $n = 3$ is used. The augmented state captures the finite memory introduced by the regression-based estimation of the PS velocity and acceleration, enabling a discrete stability analysis of the coordination algorithm.

STABILITY ANALYSIS

The force-controlled coordination algorithm creates a feedback loop between the NS and the measured displacement of the PS. The stability of the hybrid test therefore depends on the time-integration scheme, the Baumgarte stabilization parameters, and the estimation of PS velocity and acceleration. These effects are examined using the linear illustrative system as a benchmark.

Fig. 4 verifies the convergence of the coordination algorithm for different time-integration schemes. The global truncation error is evaluated after 1 ms by comparison with a reference solution computed using a sufficiently small timestep.

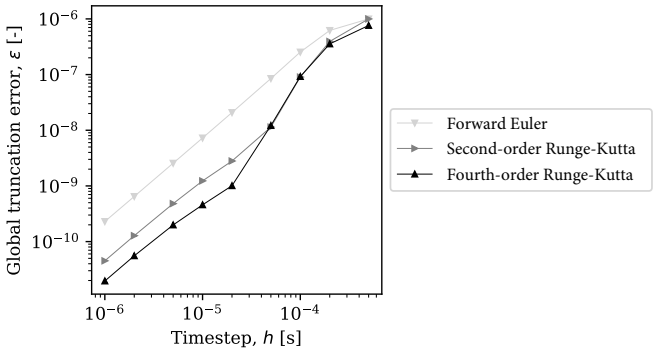

Fig. 4. Convergence analysis of global truncation error for 1 ms simulation.

The convergence results in Fig. 4 show decreasing global error for all integration schemes as the timestep is reduced. For standalone integration, the expected global errors are $O(h)$ for forward Euler, $O(h^2)$ for RK2, and $O(h^4)$ for RK4. These nominal orders are not recovered, as the

error curves have approximately the same slope. Thus, convergence is governed by the complete coordination algorithm rather than by the time integrator alone. The Baumgarte feedback terms and cubic regression of PS velocity and acceleration introduce additional approximation errors in the force command. These errors limit the practical benefit of higher-order Runge–Kutta schemes for the force-controlled hybrid test.

To determine the stable timestep range, the coordination algorithm is written as a discrete state-transition map. Stability is assessed from the spectral radius of the state-transition matrix $\mathbf{A}$,

$$\rho(\mathbf{A}) = \|\mathbf{\Lambda}\|_\infty = \max_j |\lambda_j|, \quad j = 1, \ldots, n_\lambda \tag{18}$$

where $\mathbf{\Lambda} = \mathrm{diag}(\lambda_1, \lambda_2, \ldots, \lambda_{n_\lambda})$ contains the eigenvalues of $\mathbf{A}$. The eigenvalues and eigenmodes are obtained from,

$$\mathbf{A}\boldsymbol{\varphi}_j = \lambda_j \boldsymbol{\varphi}_j, \tag{19}$$

where $\boldsymbol{\varphi}_j$ is the eigenmode associated with λ_j. The matrix $\mathbf{A}$ is the linearized state-transition matrix,

$$\mathbf{A} = \frac{\partial \mathbf{x}_{i+1}}{\partial \mathbf{x}_i}. \tag{20}$$

The spectral radius gives the stability limit, but not the numerical damping or phase error within the stable range. These quantities are extracted by expressing the dominant complex eigenvalues as,

$$\lambda = \exp\left(\omega \Delta t \left(-\xi \pm \mathrm{i}\right)\right) \tag{21}$$

where $\mathrm{i} = \sqrt{-1}$, and ω and ξ are the algorithmic frequency and damping ratio, respectively. The damping ratio ξ quantifies numerical amplitude decay, while the algorithmic frequency ω is used to compute the period distortion,

$$\Delta T = \frac{2\pi}{\omega} - T_0, \tag{22}$$

where T_0 is the period of the first eigenfrequency.

The spectral radius, numerical damping, and period distortion are shown in Fig. 5, 6 and 7,

respectively, evaluated for different time-integration schemes as a function of the nondimensional timestep,

$$\Omega = \omega_0 \Delta t, \tag{23}$$

where ω_0 is the lowest eigenfrequency of the coupled system and Δt is the integration timestep.

In contrast to the convergence analysis, the stability results show a clear difference between the integration schemes. In Fig. 5, instability occurs when $\rho > 1$. The Forward Euler scheme exceeds this limit even at the smallest timestep considered, whereas RK2 and RK4 remain stable for approximately $\Omega < 0.25$. The same trend is observed in Fig. 6, confirming the poor stability of Forward Euler and the larger stable timestep range of the Runge–Kutta schemes.

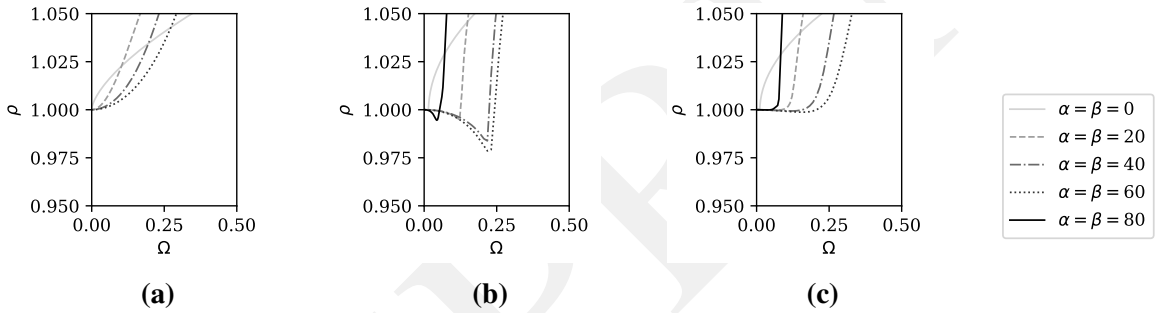

Fig. 5. Spectral radius, with instability occurring when $\rho > 1$ for a) forward Euler, b) second-order Runge–Kutta and c) fourth-order Runge–Kutta.

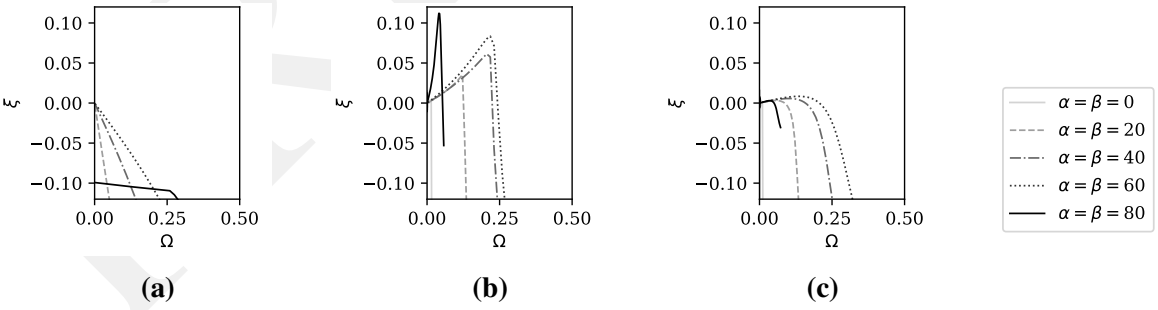

Fig. 6. Algorithmic damping ratio for a) forward Euler, b) second-order Runge–Kutta and c) fourth-order Runge–Kutta.

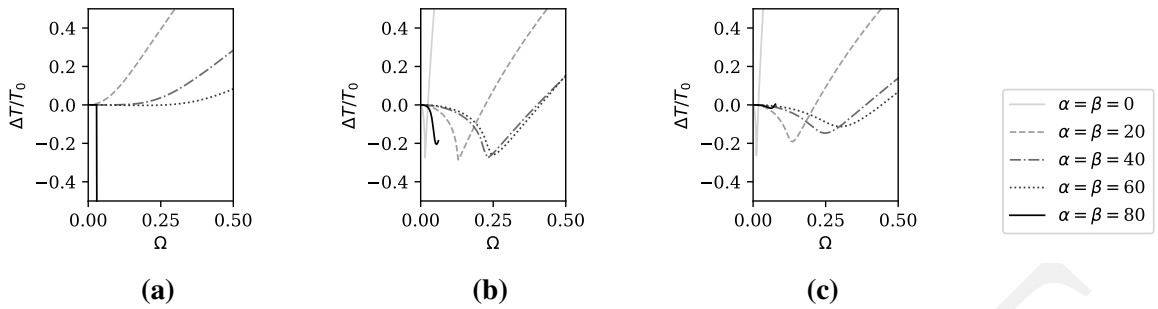

Fig. 7. Algorithmic period distortion for a) forward Euler, b) second-order Runge–Kutta and c) fourth-order Runge–Kutta.

Although RK2 and RK4 have similar stability limits, RK4 introduces less algorithmic dissipation, as shown in Fig. 6, and less algorithmic period distortion, as shown in Fig. 7.

The Baumgarte stabilization parameters influence the stability range, algorithmic dissipation, and period distortion. The results suggest an optimal parameter range, where the numerical response is least modified. Since velocity and acceleration are estimated from displacement feedback using cubic regression, the feedback loop contains memory. The observed behaviour therefore reflects the complete coordination algorithm, not the time integrator alone.

CASE STUDY: HYBRID TEST WITH A NONLINEAR NUMERICAL SUBSTRUCTURE AND STIFF PHYSICAL SUBSTRUCTURE

Hybrid model

A hybrid test is conducted for a system in which a stiff PS is coupled to a nonlinear multi-DOF NS. The hybrid model is shown in Fig. 8. The model is decomposed into the NS and PS shown in Figs. 9a and 9b, respectively. The substructures are coupled through the interface force r and the compatibility condition imposed on the PS elongation d. The NS is a two-DOF oscillator in which each DOF describes the horizontal displacement of a rigid body with mass m. A Duffing-type spring with linear stiffness k and cubic stiffness coefficient μ is connected to the first mass, while an external load f_{ext} is applied to the second mass. The PS connects the two masses and is realized by a steel bar loaded in axial extension.

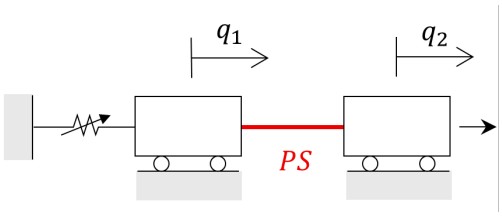

Fig. 8. Case-study hybrid model consisting of a nonlinear two-DOF NS coupled to a stiff steel-bar PS loaded in axial extension.

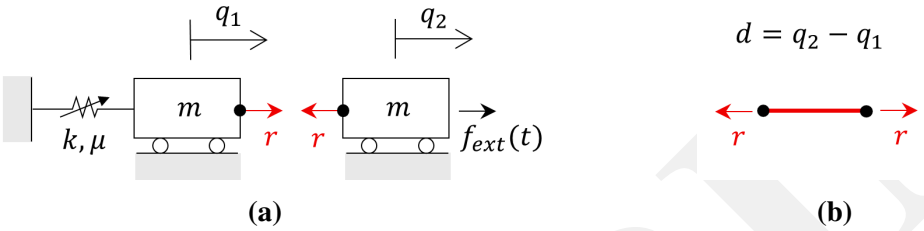

Fig. 9. Free-body diagrams of the decomposed hybrid model showing a) the numerical substructure and b) the physical substructure. The interface force r couples the two substructures, and the PS elongation d defines the displacement compatibility condition.

The PS elongation is imposed as the relative displacement between the two NS masses,

$$q_2 - q_1 = d \tag{24}$$

Using the DAE formulation in Eq. (1), the NS dynamics and interface constraint are specified by the mass matrix, force vector, and constraint mapping,

$$\mathbf{M} = \begin{bmatrix} m & 0 \\ 0 & m \end{bmatrix}, \quad \mathbf{f} = \begin{bmatrix} kq_1 + \mu q_1^3 \\ -f_{\text{ext}}(t) \end{bmatrix}, \quad \mathbf{h} = \begin{bmatrix} -1 & 1 \end{bmatrix} \tag{25}$$

where, for the case study, $m = 1000$ kg, $k = 2.33$ kN/mm, and $\mu = 36.60$ kN/mm^3. The external force $f_{\text{ext}}(t)$ is applied to the second mass as a smooth pulse with a peak amplitude of 200 N at $t = 0.1$ s. These model properties define the numerical part of the hybrid test, while the stiff PS is realized experimentally as described next.

Experimental setup

The experimental setup is a two-degree-of-freedom hybrid test bench at Aarhus University as shown in Fig. 10. The PS is a steel bar mounted in a support frame and connected to two orthogonal electromechanical actuators. Only the horizontal actuator is used here, providing a simple test case for force-controlled hybrid testing of a stiff PS.

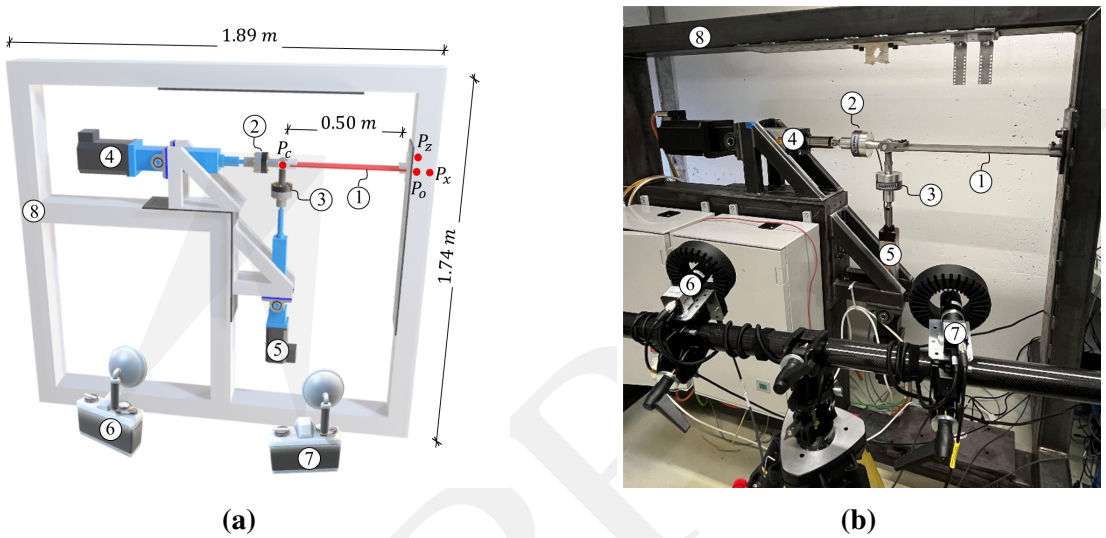

(a) **(b)**

Fig. 10. Two-degree-of-freedom hybrid test bench at Aarhus University with 1) axially loaded steel bar serving as the physical substructure, 2) and 3) force transducers, 4) and 5) electromechanical actuators, 6) and 7) cameras for 3D measurement, and 8) support steel structure.

The test bench uses two orthogonally mounted electromechanical cylinders driven by servo-motors. The horizontal actuator has a 5 mm screw lead and a nominal stroke of 100 mm; the orthogonal actuator has the same screw lead and a nominal stroke of 200 mm. The steel bar has length $l = 500$ mm and approximate axial stiffness $k_{\mathrm{PS}} = 2.9$ kN/mm.

The setup is controlled by an INDEL SAM4 real-time controller. Actuator I/O is updated through GinLink at 4 kHz, giving a control interval of 0.25 ms. Force control is implemented in INOS as a proportional load-cell feedback loop, where the actuator velocity command is adjusted to track the commanded interface force.

The hybrid-test timestep is $\Delta t = 0.5$ ms in simulation time. Because the test is pseudo-dynamic, each step is executed more slowly in wall-clock time. Camera-based displacement feedback is

acquired once per step at an average wall-clock rate of approximately 0.3 Hz.

PS displacement is measured using a calibrated Linearis3D Video photogrammetry system. The marker positions P_0, P_x, P_y, and P_c are reconstructed from synchronized camera images by triangulation (Linearis3D GmbH & Co. KG 2022). Markers P_0, P_x, and P_y define the local reference frame, while the PS elongation d is obtained from the change in distance between P_0 and P_c.

The force-controlled hybrid-test implementation is summarized in Fig. 11. The NS computes the interface force command r from the measured PS elongation d. Although the electromechanical actuator is internally displacement controlled, the commanded interface force is tracked by the outer load-cell feedback loop.

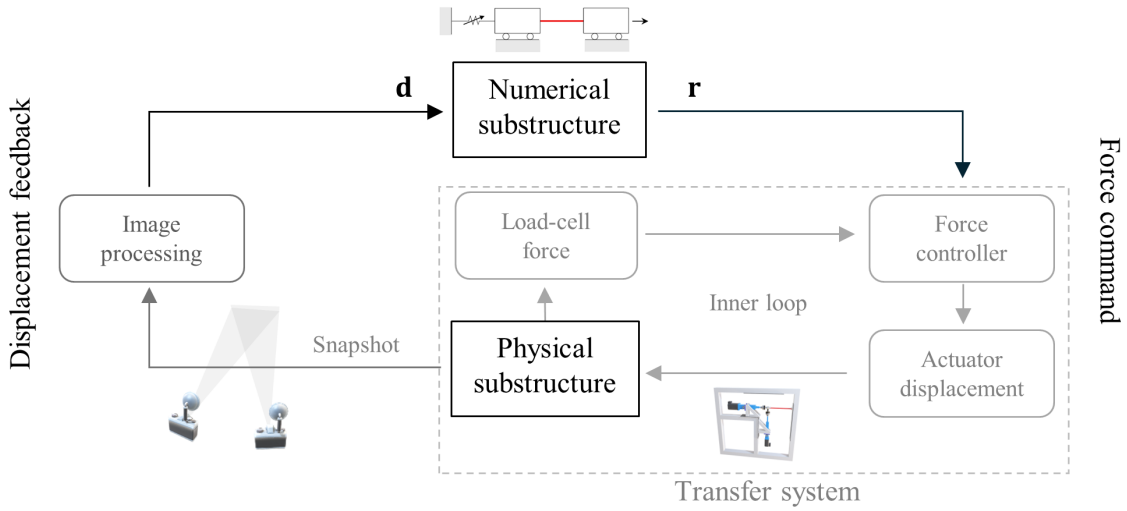

Fig. 11. Schematic overview of the force-controlled hybrid-test implementation. The NS computes the interface force command r, which is tracked by a load-cell feedback loop. The PS elongation d is obtained from camera snapshots and returned to the NS as displacement feedback.

The hybrid test used Baumgarte parameters $\alpha = \beta = 60\ \mathrm{s}^{-1}$. PS derivatives were estimated by cubic regression using the three most recent simulated displacement–velocity states and the current measured displacement. The resulting coupled response, interface compatibility, and force–displacement behavior are evaluated next.

RESULTS AND DISCUSSION

The hybrid-test response is evaluated through the NS motion, interface compatibility, and force–displacement behavior. Fig. 12 compares the NS coordinates q_1 and q_2 with the reference simulation, while Fig. 13 shows the measured PS elongation d against the relative NS displacement. The stiff-PS response is assessed from the force–displacement relation in Fig. 14, and the nonlinear NS behavior from the Duffing restoring-force relation in Fig. 15.

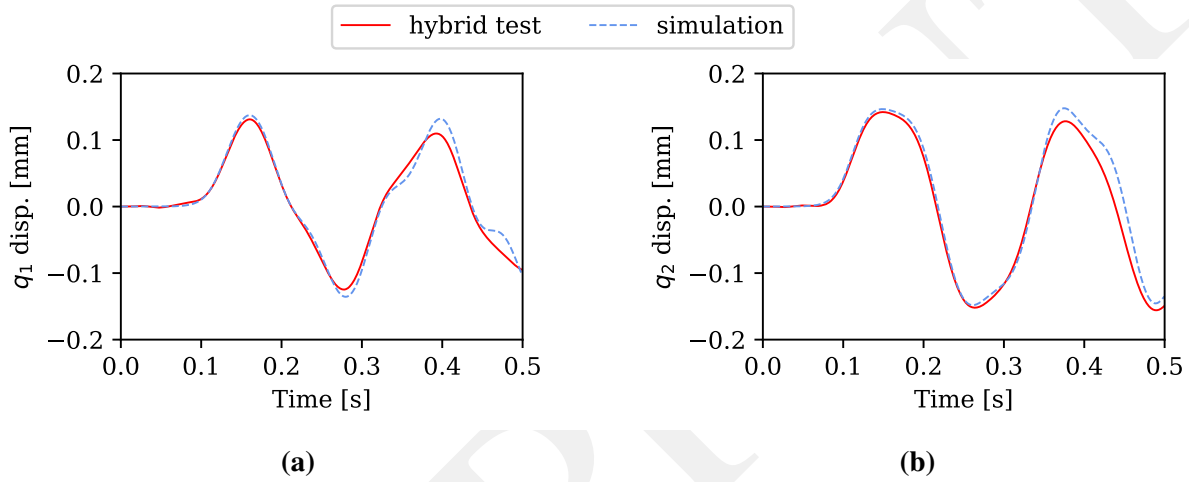

Fig. 12. Time response of the NS coordinates comparing the hybrid-test response with the reference simulation for a) displacement q_1 and b) displacement q_2.

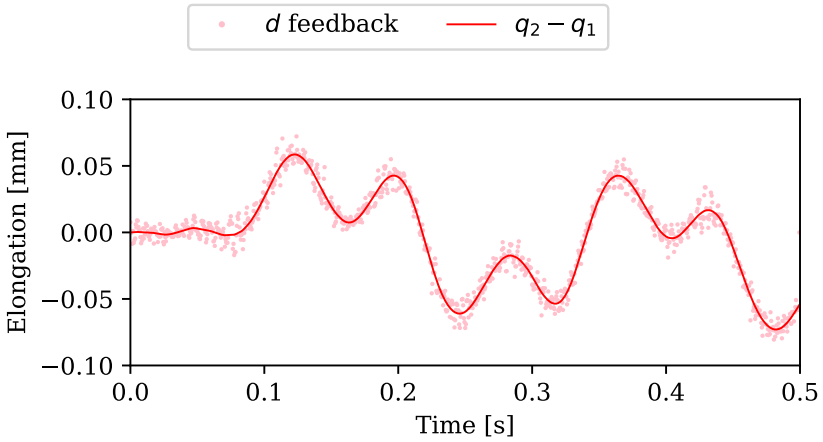

Fig. 13. Measured PS elongation during the hybrid test compared with the relative NS displacement $q_2 - q_1$.

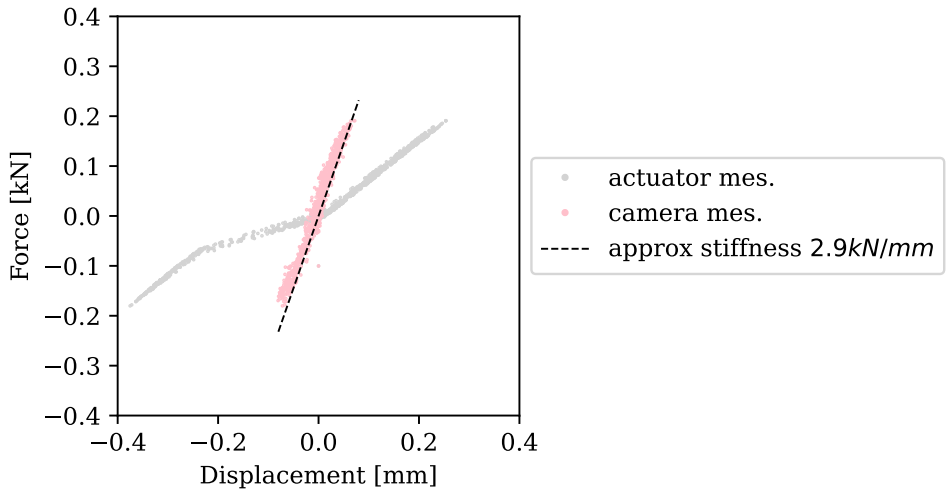

Fig. 14. Measured force–displacement response of the stiff PS comparing actuator-based displacement and camera-based specimen elongation.

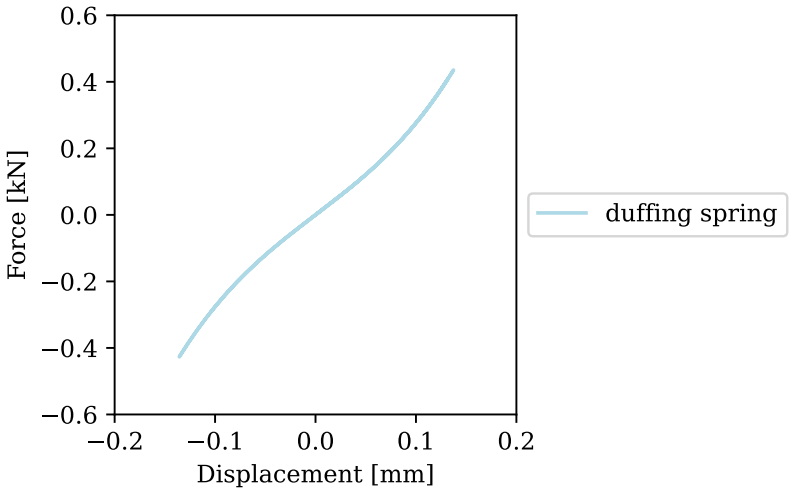

Fig. 15. Nonlinear force-displacement relation of the Duffing spring in the NS.

The behavior of the hybrid test is quantified using performance indices adapted from the hybrid testing criteria proposed in (Silva et al. 2020),

$$J_1 = \sqrt{\frac{\sum_{i=1}^{N} [\mathbf{hq}(t_i) - d(t_i)]^2}{\sum_{i=1}^{N} [d(t_i)]^2}} = 17.18\ \% \tag{26}$$

$$J_2 = \sqrt{\frac{\sum_{i=1}^{N}[q_1(t_i) - q_1^{\mathrm{ref}}(t_i)]^2}{\sum_{i=1}^{N}[q_1^{\mathrm{ref}}(t_i)]^2}} = 15.34\ \% \tag{27}$$

$$J_3 = \sqrt{\frac{\sum_{i=1}^{N}[q_2(t_i) - q_2^{\mathrm{ref}}(t_i)]^2}{\sum_{i=1}^{N}[q_2^{\mathrm{ref}}(t_i)]^2}} = 17.68\ \% \tag{28}$$

The hybrid test remains stable and reproduces the dominant dynamics of the reference simulation. The NS coordinates q_1 and q_2 in Fig. 12 show bounded oscillatory responses without visible amplitude growth. The hybrid-test trajectories reproduce the main phase and amplitude of the reference response, with normalized errors of $J_2 = 15.34$ % for q_1 and $J_3 = 17.68$ % for q_2. These errors are considered acceptable for this proof-of-concept test because they remain bounded and do not introduce drift or instability. The mismatch is mainly attributed to displacement-feedback noise, derivative-estimation error, transfer-system compliance, and imperfect force tracking. This indicates that the force-controlled coupling preserves the main coupled response without destabilizing the hybrid system.

The Baumgarte-stabilized constraint introduces small feedback oscillations, but these do not destabilize the response. In Fig. 13, the measured PS elongation d follows the relative NS displacement $q_2 - q_1$, while showing small oscillations around the hybrid-test response. The normalized compatibility error is $J_1 = 17.18$ %, but no drift is observed during the test, and the oscillations do not propagate into growing amplitudes in q_1 or q_2. This suggests that the Baumgarte terms act as a soft constraint correction. The compatibility error is regulated gradually, making the force command less sensitive to noise in the displacement feedback.

The actuator displacement does not represent the true elongation of the stiff PS. Fig. 14 shows a clear difference between the actuator-based and camera-based force–displacement curves. The camera measurement gives the local specimen elongation and follows an approximately linear stiffness of about 2.9 kN/mm, whereas the actuator displacement includes additional deformation from the transfer system. This shows that the transfer-system compliance is not negligible compared with the deformation of the stiff PS. Independent displacement feedback is therefore needed, and

the result supports the use of force control for stiff physical substructures.

The method couples the stiff experimental PS to a nonlinear NS. Fig. 15 shows the nonlinear Duffing restoring-force relation, while Figs. 12 and 13 show that the coupled response remains stable. This confirms that the formulation can handle nonlinear numerical-substructure dynamics.

The remaining mismatch reflects the sensitivity of the coordination scheme to timestep selection, Baumgarte stabilization, derivative estimation, and measurement noise. The timestep must remain within the stable range identified in the linear analysis, while the Baumgarte parameters balance constraint enforcement against noise sensitivity. In addition, the cubic-regression derivative estimates introduce approximation errors and may amplify noisy displacement feedback. These coupled effects must therefore be tuned jointly.

CONCLUSION

This paper presented a DAE-based coordination method for force-controlled hybrid testing of stiff physical substructures coupled to nonlinear numerical substructures. Displacement compatibility was imposed as an algebraic constraint, and the interface force was obtained using Baumgarte-stabilized Lagrange multipliers.

Since physical-substructure velocity and acceleration are not measured directly in pseudo-dynamic testing, they were estimated from displacement feedback. In the present implementation, cubic regression introduced finite memory into the feedback loop. Consequently, the nominal convergence orders of the standalone time integrators were not recovered, and stability and convergence depended on the complete coordination algorithm.

The linear benchmark showed that the stable timestep range depends on the integration scheme, Baumgarte parameters, and derivative estimation. For the selected parameters, RK2 and RK4 remained stable for approximately $\Omega < 0.25$, while Forward Euler was unstable over the investigated range. RK4 introduced less numerical damping and period distortion than RK2.

The experimental test demonstrated stable force-controlled coupling between a stiff steel-bar physical substructure and a nonlinear two-DOF numerical substructure. The response remained bounded and maintained displacement compatibility without drift. Camera-based elongation mea-

surement was required because actuator displacement included transfer-system compliance.

Future work should address the joint effect of derivative estimation and Baumgarte stabilization in pseudo-dynamic force-controlled hybrid tests.

CREDIT AUTHORSHIP CONTRIBUTION STATEMENT

F. Nordtorp: Writing – review & editing, Writing – original draft, Visualization, Investigation, Formal analysis, Validation, Software, Methodology, Conceptualization. **G. Abbiati**: Writing – review & editing, Project administration, Supervision, Methodology, Conceptualization.

DATA AVAILABILITY STATEMENT

Some or all data, models, or code that support the findings of this study are available from the corresponding author upon reasonable request.

ACKNOWLEDGMENTS

This research was funded by EUDP – the Energy Technology Development and Demonstration Program – through the following projects:

- Project 64019-0595 DLTE, a collaboration between Aarhus University, Department of Electrical and Computer Engineering and Department of Civil and Architectural Engineering (AU-ECE, AU-CAE), R&D Test Systems A/S, and FORCE Technology.
- Project 640222-497272 DIGIT-BENCH, a collaboration between Aarhus University, Department of Electrical and Computer Engineering and Department of Civil and Architectural Engineering (AU-ECE, AU-CAE), R&D Test Systems A/S, and Lindø Offshore Renewable Center (LORC).

REFERENCES

Abbiati, G., Bursi, O. S., Caperan, P., Di Sarno, L., Molina, F. J., Paolacci, F., and Pegon, P. (2015). "Hybrid simulation of a multi-span rc viaduct with plain bars and sliding bearings." *Earthquake Engineering & Structural Dynamics*, 44(13), 2221–2240.

Ascher, U. M. and Petzold, L. R. (1998). *Computer Methods for Ordinary Differential Equations and Differential-Algebraic Equations*. Society for Industrial and Applied Mathematics, USA, 1st edition.

Bas, E. E. and Moustafa, M. A. (2020a). "Performance and limitations of real-time hybrid simulation with nonlinear computational substructures." *Experimental Techniques*, 44, 715–734.

Bas, E. E. and Moustafa, M. A. (2020b). "Real-time hybrid simulation with deep learning computational substructures: System validation using linear specimens." *Machine Learning and Knowledge Extraction*, 2(4), 469–489.

Baumgarte, J. (1972). "Stabilization of constraints and integrals of motion in dynamical systems." *Computer Methods in Applied Mechanics and Engineering*, 1(1), 1–16.

Belloli, M., Bayati, I., Facchinetti, A., Fontanella, A., Giberti, H., La Mura, F., Taruffi, F., and Zasso, A. (2020). "A hybrid methodology for wind tunnel testing of floating offshore wind turbines." *Ocean Engineering*, 210, 107592.

Bursi, O. S., Wang, Z., Jia, C., et al. (2013). "Monolithic and partitioned time integration methods for real-time heterogeneous simulations." *Computational Mechanics*, 52, 99–119.

Carl, J. and Sivaselvan, M. V. (2011). "Improved dynamic testing by impedance control." *Earthquake Engineering and Engineering Vibration*, 10(3), 423–435.

Carrion, J. E. and Spencer, Billie F., J. (2007). "Model-based strategies for real-time hybrid testing." *NSEL Report Series NSEL-006*, Newmark Structural Engineering Laboratory, Department of Civil and Environmental Engineering, University of Illinois at Urbana-Champaign, Urbana, IL (December). UILU-ENG-2007-1806; ISSN 1940-9826.

Chen, P.-C., Hsu, S.-C., and Ma, C.-C. (2024). "Development and verification of real-time hybrid simulation with deep learning-based nonlinear numerical substructure." *Earthquake Engineering & Structural Dynamics*, 53(6), 2141–2161.

Christenson, R., Lin, Y. Z., Emmons, A., and Bass, B. (2008). "Large-scale experimental verification of semiactive control through real-time hybrid simulation1." *Journal of Structural Engineering*, 134(4), 522–534.

Dimig, J., Shield, C., Bailey, F., and Clark, A. (1999). "Effective force testing: A method of seismic simulation for structural testing." *Journal of Structural Engineering*, 125.

Ding, H., Zhang, Z., Wang, J., Zhang, J., and Altay, O. (2024). "Multiscale fluid–structure coupled real-time hybrid simulation of monopile wind turbines with vibration control devices." *Mechanical Systems and Signal Processing*, 215, 111439.

Fermandois, G. and Spencer, B. F. (2017). "Model-based framework for multi-axial real-time hybrid simulation testing." *Earthquake Engineering and Engineering Vibration*, 16(4), 671–691.

Forouzan, B. and Nakata, N. (2015). "A new force-based algorithm for hybrid simulation." *Proceedings of the 6th International Conference on Advances in Experimental Structural Engineering and the 11th International Workshop on Advanced Smart Materials and Smart Structures Technology*, Urbana-Champaign, IL, USA (August). August 1–2, 2015.

Guo, W., Zeng, C., Gou, H., Gu, Q., Wang, T., Zhou, H., Zhang, B., and Wu, J. (2021). "Real-time hybrid simulation of high-speed train-track-bridge interactions using the moving load convolution integral method." *Engineering Structures*, 228, 111537.

Hakuno, M., Shidawara, M., and Hara, T. (1969). "Dynamic destructive test of a cantilever beam, controlled by an analog-computer." *Proceedings of the Japan Society of Civil Engineers*, 1969(171), 1–9.

Herrmann, S., Kaehler, M., Souffrant, R., Rachholz, R., Zierath, J., Kluess, D., Mittelmeier, W., Woernle, C., and Bader, R. (2012). "Hil simulation in biomechanics: A new approach for testing total joint replacements." *Computer Methods and Programs in Biomedicine*, 105(2), 109–119.

Jia, C., Bursi, O. S., Bonelli, A., and Wang, Z. (2011). "Novel partitioned time integration methods for dae systems based on l-stable linearly implicit algorithms." *International Journal for Numerical Methods in Engineering*, 87(12), 1148–1182.

Kolay, C., Ricles, J. M., Marullo, T. M., Mahvashmohammadi, A., and Sause, R. (2015). "Implementation and application of the unconditionally stable explicit parametrically dissipative kr-α method for real-time hybrid simulation." *Earthquake Engineering & Structural Dynamics*, 44(5), 735–755.

Linearis3D GmbH & Co. KG (2022). *Linearis3D Video User Manual*. Linearis3D GmbH & Co. KG, Braunschweig, Germany, version 2.0 edition (September).

Liu, H., Tang, Z., and Enokida, R. (2024a). "Stability prediction method of time-varying real-time hybrid testing system on vehicle-bridge coupled system." *Mechanical Systems and Signal Processing*, 216, 111463.

Liu, J., Silva, C. E., Dyke, S. J., Wu, Y., and Liu, H. (2024b). "Using real-time hybrid simulation for active mass damper experimentation and validation." *Mechanism and Machine Theory*, 191, 105474.

Mosqueda, G. and Ahmadizadeh, M. (2011). "Iterative implicit integration procedure for hybrid simulation of large nonlinear structures." *Earthquake Engineering & Structural Dynamics*, 40(9), 945–960.

Neumann, C. et al. (2023). "Hydrodynamic real-time hybrid simulation demonstrated for wave–structure interaction." *Journal of Waterway, Port, Coastal, and Ocean Engineering*.

Ou, G., Ozdagli, A. I., Dyke, S. J., and Wu, B. (2015). "Robust integrated actuator control: experimental verification and real-time hybrid-simulation implementation." *Earthquake Engineering & Structural Dynamics*, 44(3), 441–460.

Pan, P., Wang, T., and Nakashima, M. (2016). *Development of online hybrid testing: theory and applications to structural engineering*. Elsevier / Butterworth Heinemann, Oxford [England] ; Waltham, MA.

Pratt, J. and Krupp, B. (2004). "Series elastic actuators for legged robots." *Proceedings of SPIE - The International Society for Optical Engineering*.

Saouma, V. and Sivaselvan, M. (2014). *Hybrid simulation: Theory, implementation and applications*. CRC Press.

Sauca, A., Mortensen, N., Drustrup, A., and Abbiati, G. (2021). "Experimental validation of a hybrid fire testing framework based on dynamic relaxation." *Fire Safety Journal*, 121, 103315.

Sauder, T., Chabaud, V., Thys, M., Bachynski, E. E., and Sæther, L. O. (2016). "Real-time hybrid model testing of a braceless semi-submersible wind turbine: Part i — the hybrid approach."

Volume 6: Ocean Space Utilization; Ocean Renewable Energy, V006T09A039.

Shao, P., Guo, W., Lei, Q., and Zeng, C. (2021). "Adaptive compound control for the real-time hybrid simulation of high-speed railway train–bridge coupling vibration." *Structural Control and Health Monitoring*, 28.

Silva, C. E., Gomez, D., Maghareh, A., Dyke, S. J., and Spencer, B. F. (2020). "Benchmark control problem for real-time hybrid simulation." *Mechanical Systems and Signal Processing*, 135, 106381.

Sivaselvan, M. V., Reinhorn, A. M., Shao, X., and Weinreber, S. (2008). "Dynamic force control with hydraulic actuators using added compliance and displacement compensation." *Earthquake Engineering & Structural Dynamics*, 37(15), 1785–1800.

Stefanaki, A. and Sivaselvan, M. V. (2018). "A simple strategy for dynamic substructuring: I. Concept and development." *Earthquake Engineering & Structural Dynamics*, 47(9), 1801–1822.

Su, W. and Song, W. (2019). "A real-time hybrid aeroelastic simulation platform for flexible wings." *Aerospace Science and Technology*, 95, 105513.

Takanashi, K., Udagawa, K., Seki, M., Okada, T., and Tanaka, H. (1975). "Non-linear earthquake response analysis of structures by a computer-actuator on-line system." *Transaction of the Architectural Institute of Japan*, 229, 77–83.

Verma, M., Sivaselvan, M. V., and Rajasankar, J. (2019). "Impedance matching for dynamic substructuring." *Structural Control and Health Monitoring*, 26(11).

Witteveen, W. and Koller, L. (2023). "Frf-based non-simultaneous real-time hybrid testing of multiple subsystems with moderate nonlinearities." *Mechanical Systems and Signal Processing*, 188, 109944.

Zhang, Z., Staino, A., Basu, B., and Nielsen, S. R. (2016). "Performance evaluation of full-scale tuned liquid dampers (tlds) for vibration control of large wind turbines using real-time hybrid testing." *Engineering Structures*, 126, 417–431.

Zhao, J., Shield, C., French, C., and Posbergh, T. (2005). "Nonlinear system modeling and velocity feedback compensation for effective force testing." *Journal of Engineering Mechanics*, 131(3),

244–253.

Zhou, H., Wagg, D. J., and Li, M. (2017). “Equivalent force control combined with adaptive polynomial-based forward prediction for real-time hybrid simulation.” *Structural Control and Health Monitoring*, 24(11), e2018 e2018 STC-16-0051.R2.